CHAPTER 5

Stator Voltage Vector Control of Doubly-Fed Induction Generator using Back-to-Back Three-Level Neutral Point Clamped Voltage Source Converter

5.1 Introduction

The vector control of the DFIG with the stator connected to the utility grid and the rotor supplied with back-to-back three-level NPC VSC will be presented in this chapter. The control strategy is based on the stator voltage vector control technique. This chapter analyzes the concept of the proposed scheme. The converters are controlled using stator/grid voltage vector control techniques and the grid-connected operation has been considered. The control strategy enables the independent current control of the electromagnetic torque and the reactive power. The simulation results for 1kW/380V/50Hz DFIG variable-speed system validate the proposed topology and control scheme. Sub-synchronous and super-synchronous operations of the grid-connected have been verified and transition through synchronous speed has been achieved.

5.2 DFIG system with back-to-back three-level NPC VSC

The typical scheme of the proposed DFIG system is shown in Figure 5.1. A control scheme of the DFIG system using back-to-back three-level NPC VSC is proposed. The proposed control scheme for the rotor-side converter is based on the stator voltage vector control technique, which can be controlled overall power factor of DFIG system. The control scheme for the grid-side converter uses the standard grid-connected vector control.

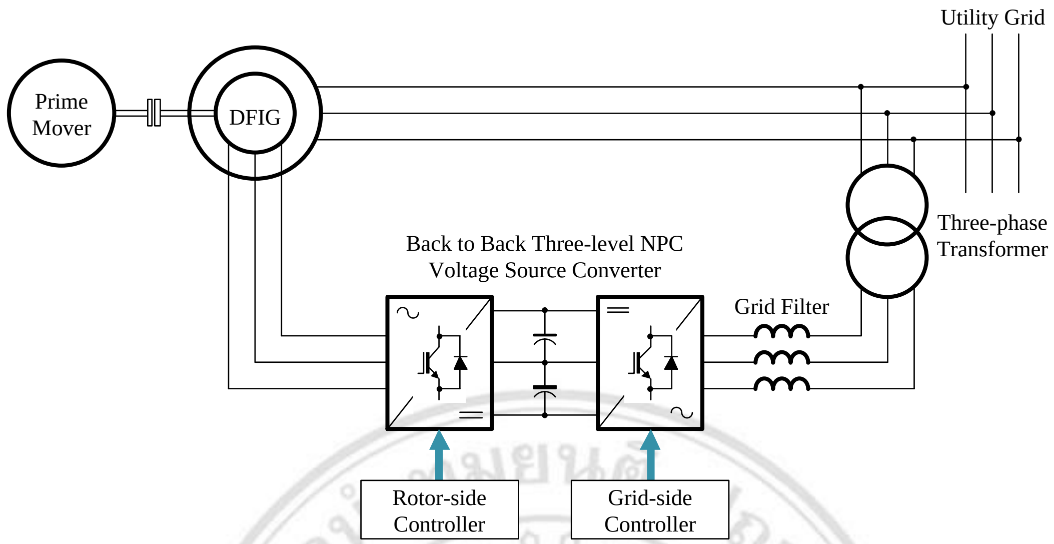

Figure 5.1 Configuration for the DFIG system using back-to-back three-level NPC VSC.

5.3 Rotor-side converter controlled of DFIG system

5.3.1 Stator voltage vector control principle

Traditionally, the techniques to control the rotor-side converter of DFIG system are the stator flux vector control, which the reference frame has to be aligned with the stator flux linkage [11]. In this thesis, the stator voltage vector will be is referred to as stator voltage orientation, which is aligned with stator voltage.

Stator voltage vector control has been implemented in the experimental setup. Figure 5.2 shows a relationship between the stationary reference frame and stator voltage vector reference frame for the DFIG. The stator voltage vector control is achieved by aligning the *d*-axis of the rotating reference frame. Therefore, the stator voltage equations in *d*-*q* rotating reference frame can be expressed as

$$v_{sd} = |v_s|,\ v_{sq} = 0, \tag{5.1}$$

where v_{sd} and v_{sq} are the stator voltage components in the rotating reference frame.

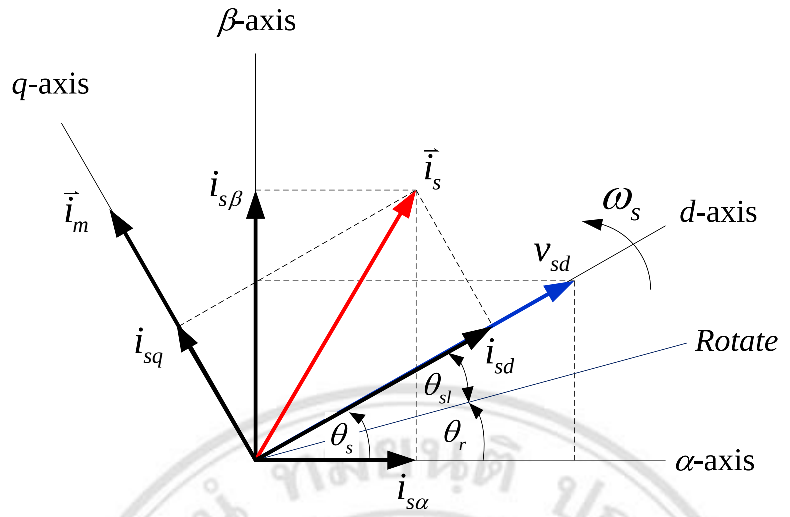

Figure 5.2 Vector diagram between the stationary reference frame and stator voltage vector reference frame.

In the stator voltage vector frame, the magnetizing current $\vec{i}_m$ can be considered constant, which is expressed as:

$$\vec{i}_m = \frac{\vec{v}_s}{j\omega_s L_m}, \tag{5.2}$$

and can be decomposed into the d and q components:

$$\begin{cases} i_{md} = \dfrac{v_{sq}}{\omega_s L_m} = 0, \\ i_{mq} = -\dfrac{v_{sd}}{\omega_s L_m}. \end{cases} \tag{5.3}$$

where i_{md} and i_{mq} are the magnetizing current components in the rotating reference frame.

In the stator voltage reference frame, the stator flux vector $\vec{\lambda}_s$ equation can be given as

$$\vec{\lambda}_s = L_s \vec{i}_s + L_m \vec{i}_r = L_m \vec{i}_m. \tag{5.4}$$

Therefore, the stator flux linkage components $\lambda_{sd}, \lambda_{sq}$ can be expressed as

$$\begin{cases} \lambda_{sd} = L_m i_{md} = 0, \\ \lambda_{sq} = L_m i_{mq} = -\dfrac{v_{sd}}{\omega_s}. \end{cases} \tag{5.5}$$

The rotor flux vector $\vec{\lambda}_r$ in the stator voltage reference frame can be expressed as

$$\vec{\lambda}_r = L_r \vec{i}_r + L_m \vec{i}_s = L_r \vec{i}_r + \frac{L_m^2}{L_s}\left(\vec{i}_m - \vec{i}_r\right). \tag{5.6}$$

Consequently, the rotor flux linkage components $\lambda_{rd}, \lambda_{rq}$ can be expressed as

$$\begin{cases} \lambda_{rd} = \sigma L_r i_{rd}, \\ \lambda_{rq} = \sigma L_r i_{rq} + \dfrac{L_m^2}{L_s} i_m. \end{cases} \tag{5.7}$$

From the voltage equations of the DFIG in (4.1) is applied to stator voltage vector control. Therefore, the stator voltage equations in *d*-*q* rotating reference frame is given by

$$\begin{cases} v_{sd} = R_s i_{sd} - \omega_s L_m i_{mq}, \\ v_{sq} = 0, \end{cases} \tag{5.8}$$

and the rotor voltage equations in *d*-*q* rotating reference frame is given by

$$\begin{cases} v_{rd} = R_r i_{rd} + \sigma L_r \dfrac{d}{dt} i_{rd} - \omega_{sl}\left(\sigma L_r i_{rq} - \dfrac{v_{sd} L_m}{\omega_s L_s}\right), \\ v_{rq} = R_r i_{rq} + \sigma L_r \dfrac{d}{dt} i_{rq} + \omega_{sl} \sigma L_r i_{rd}. \end{cases} \tag{5.9}$$

The electromagnetic torque T_e equation in terms of the rotor current is given by

$$T_e = -\frac{3}{2} p_p \frac{L_m}{\omega_s L_s} v_{sd} i_{rd}. \quad (5.10)$$

From (5.10), the electromagnetic torque is therefore proportional to the *d*-axis rotor current.

Considering (4.4) in Chapter 4, neglecting the power losses associated with the stator resistances and under stator voltage orientation, the stator active and reactive powers are given by

$$\begin{cases} P_s = \frac{3}{2} v_{sd} i_{sd} = -\frac{3}{2} \frac{L_m}{L_s} v_{sd} i_{rd}, \\ Q_s = -\frac{3}{2} v_{sd} i_{sq} = -\frac{3}{2} \frac{L_m}{L_s} v_{sd} \left(i_{mq} - i_{rq} \right). \end{cases} \quad (5.11)$$

The above equations show the independent control of the stator active and reactive power flow can be achieved. The *q*-axis rotor current component i_{rq} can be controlled the reactive power flow into the utility grid. It can be adjusted to make the generator operating at unity power factor.

5.3.2 Stator voltage vector control scheme

The structure of rotor-side converter control in stator voltage vector control is shown in Figure 5.3. The current control loops implement the effective control of the stator active and reactive powers of the DFIG. The stator active and reactive powers are independently regulated by the decoupled rotor current controllers in *d*-*q* rotating reference frame. The *d*-*q* axis current references i_{rd}^*, i_{rq}^* are calculated by

$$\begin{cases} i_{rd}^* = -\frac{2}{3} \frac{\omega_s L_s}{v_{sd} L_m p_p} T_e^*, \\ i_{rq}^* = \frac{2}{3} \frac{L_s}{v_{sd} L_m} Q_s^* - \frac{v_{sd}}{\omega_s L_m}. \end{cases} \quad (5.12)$$

Next, the outputs of the rotor current controllers are the voltage references in the rotating reference frame v_{Lrd}^{*}, v_{Lrq}^{*}. The compensations correspond to the rotor voltage signals and the decoupling terms of the *d*-*q* axis rotor current components. Therefore, the reference rotor voltages v_{rd}^{*}, v_{rq}^{*} are expressed as

$$\begin{cases} v_{rd}^{*} = v_{Lrd}^{*} - \omega_{sl}\left(\sigma L_r i_{rq} - \dfrac{v_{sd} L_m}{\omega_s L_s}\right), \\ v_{rq}^{*} = v_{Lrq}^{*} + \omega_{sl}\sigma L_r i_{rd}. \end{cases} \tag{5.13}$$

The reference rotor voltages are transformed into the *abc* reference frame. Finally, the PWM signals are generated by the modified SVPWM technique, which generates switching signals for rotor-side three-level NPC VSC.

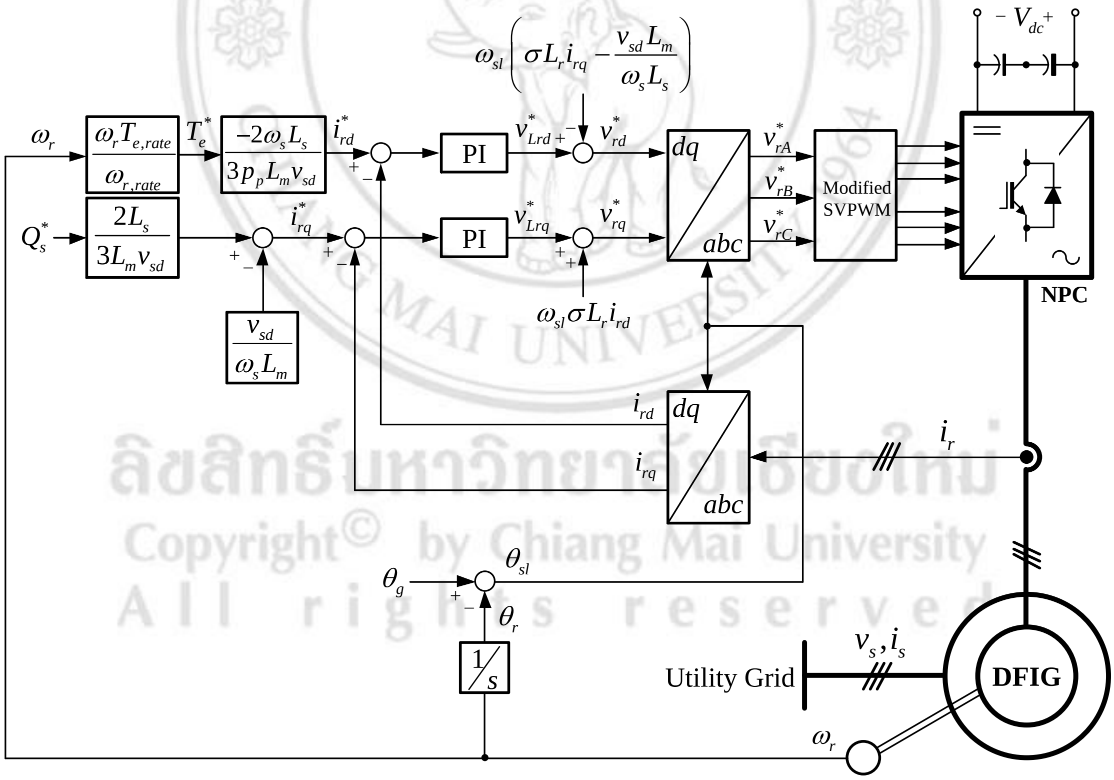

Figure 5.3 Block diagram of rotor-side three-level NPC VSC controlled for DFIG system.

5.3.3 Design of rotor current controller

The d-axis and q-axis rotor current controller have the same dynamic controls. Considering (5.13) with the d-axis of rotating reference frame aligned in the stator voltage vector, the rotor inductance reference voltages v_{Lrd}^*, v_{Lrq}^* are specified as

$$\begin{cases} v_{Lrd}^* = R_r i_{rd} + \sigma L_r \dfrac{d}{dt} i_{rd}, \\ v_{Lrq}^* = R_r i_{rq} + \sigma L_r \dfrac{d}{dt} i_{rq}. \end{cases} \tag{5.14}$$

By Laplace transform, the rotor inductance voltage equations can be expressed as

$$\begin{aligned} v_{Lrd}^*(s) &= R_r i_{rd}(s) + \sigma L_r s i_{rd}(s) \\ v_{Lrq}^*(s) &= R_r i_{rq}(s) + \sigma L_r s i_{rq}(s) \end{aligned} \tag{5.15}$$

The transfer function of the rotor current loop can be written as

$$\frac{i_{rd}(s)}{v_{Lrd}^*(s)} = \frac{i_{rq}(s)}{v_{Lrq}^*(s)} = \frac{1}{R_r + \sigma L_r s} \tag{5.16}$$

Equation (5.16) shows that the relationship between rotor currents and the rotor inductance voltages is equivalent to a first order system. The PI controller for achieving good performance of tracking the d-q reference current signals can be synthesized for the desired closed-loop transfer function.

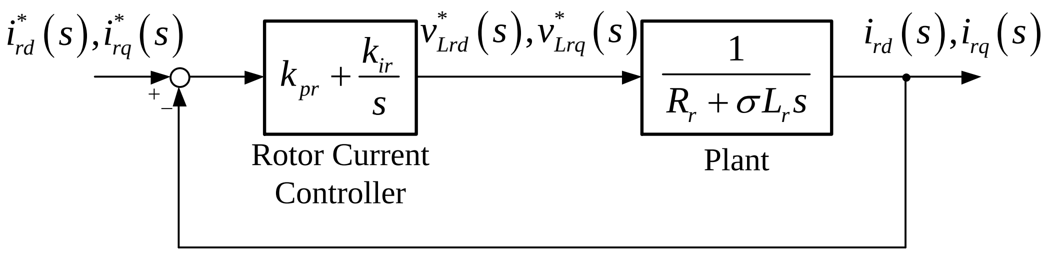

Figure 5.4 Block diagram of the rotor current control loop.

Therefore, the closed-loop transfer function of the rotor current controller in Figure 5.4 can be written as

$$\frac{i_{rd}^{*}(s)}{i_{rd}(s)} = \frac{i_{rq}^{*}(s)}{i_{rq}(s)} = \frac{\dfrac{k_{pr}s + k_{ir}}{\sigma L_r}}{s^2 + \dfrac{R_r + k_{pr}}{\sigma L_r}s + \dfrac{k_{ir}}{\sigma L_r}}. \tag{5.17}$$

The general form of the characteristic equation of the second-order system for the rotor current controller is given by

$$s^2 + 2\xi\omega_{nr}s + \omega_{nr}^2 = 0, \tag{5.18}$$

where ω_{nr} is the natural angular frequency of current control for $\xi \le 1$ and ξ is the damping ratio.

Therefore, the parameters of PI controller of rotor current control can be calculated as

$$\begin{cases} k_{pr} = 2\xi\omega_{nr}\sigma L_r - R_r, \\ k_{ir} = \omega_{nr}^2\sigma L_r. \end{cases} \tag{5.19}$$

5.4 Grid-side converter controlled of DFIG system

The most popular structure proposed as a converter is the diode-clamped converter based on the neutral-point converter presented in [23]. Therefore, when comparing to a conventional two-level VSC topology, the three-level NPC VSC are the most suitable power converters for high power medium voltage applications. It increases the output voltage magnitude, reduces the output voltage and current harmonic distortion. However, this topology has some drawbacks such as additional clamping diodes, complicated PWM switching pattern design and possible deviation of the dc-link voltage unbalance.

5.4.1 Grid-connected voltage vector control principle

The objective of the grid-side converter is based on the decoupled voltage vector control concept, to maintain a constant dc-link voltage, either by feeding the active power into the grid or by consuming active power from the grid, depending on the speed of the DFIG. Traditionally, the grid-connected converter can be used to produce active and reactive power with the controlled *d-q* axis current components, respectively.

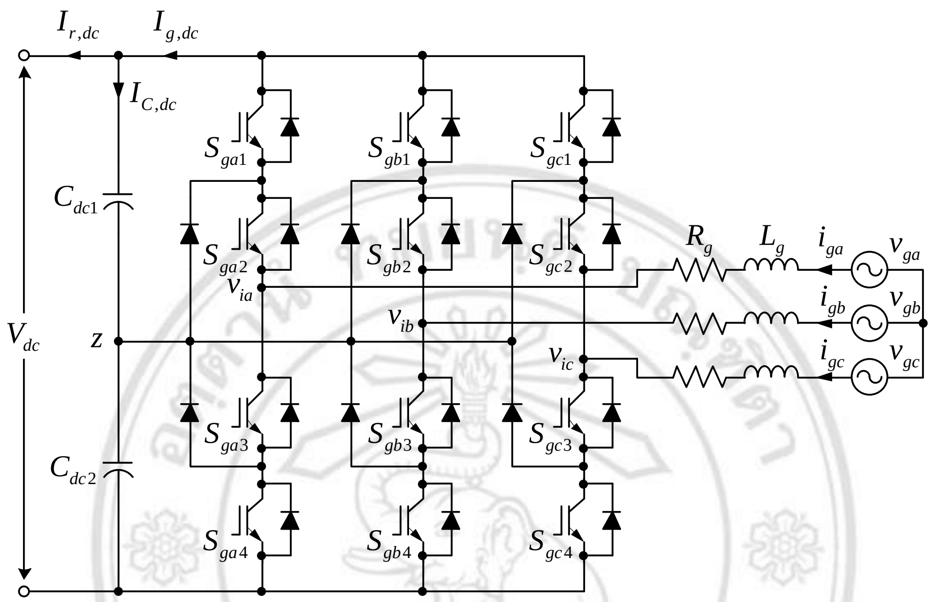

Figure 5.5 Equivalent circuit of the grid-connected three-level NPC VSC.

Figure 5.5 shows the simplified equivalent circuit of the grid-connected three-level NPC VSC. The converter consists of twelve active switches and six anti-parallel diodes. The three-level NPC VSC ac supply side is connected using three inductor L_g with loss resistor R_g for inject current to cancel the harmonic component current. The dc-link voltage V_{dc} must be regulated and balanced. In this figure, assuming ideal commutation and neglecting the effect of harmonics, the voltage equations that model the grid-connected three-level NPC VSC can be derived as follow:

$$\begin{cases} v_{ga} = R_g i_{ga} + L_g \dfrac{d}{dt} i_{ga} + v_{ia}, \\ v_{gb} = R_g i_{gb} + L_g \dfrac{d}{dt} i_{gb} + v_{ib}, \\ v_{gc} = R_g i_{gc} + L_g \dfrac{d}{dt} i_{gc} + v_{ic}, \end{cases} \tag{5.20}$$

where v_{ga}, v_{gb}, v_{gc} are the phase grid voltages, v_{ia}, v_{ib}, v_{ic} are the phase grid-side converter voltages, i_{ga}, i_{gb}, i_{gc} are phase grid currents, R_g is resistance of utility grid and L_g is inductance of utility grid or utility grid filter.

A dynamic mathematical model of grid-side converter is developed in its original three-phase *abc* frame. This three-phase model is transformed into the *d*-*q* rotating reference frame. From (5.20), the output voltages of the utility grid in the rotating reference frame are expressed by,

$$\begin{cases} v_{gd} = R_g i_{gd} + L_g \dfrac{d}{dt} i_{gd} - \omega_g L_g i_{gq} + v_{id}, \\ v_{gq} = R_g i_{gq} + L_g \dfrac{d}{dt} i_{gq} + \omega_g L_g i_{gd} + v_{iq}. \end{cases} \tag{5.21}$$

where v_{gd}, v_{gq} are the *d*-*q* axis grid voltages, v_{id}, v_{iq} are the *d*-*q* axis grid-side converter voltages, i_{gd}, i_{gq} are the the *d*-*q* axis grid currents.

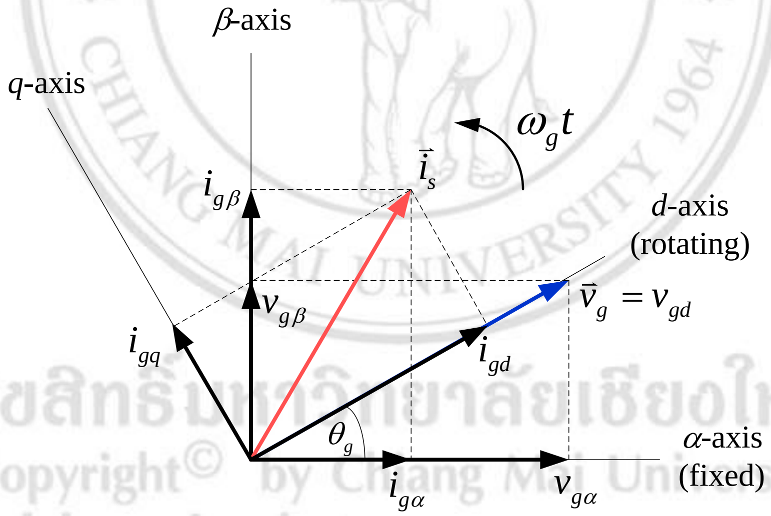

Figure 5.6 Phasor diagram of the grid-connected three-level NPC VSC.

The phasor diagram for vector control of the grid-connected VSC is shown in Figure 5.6 by placing the *d*-axis of the rotating reference frame on the utility grid voltage vector, v_{gq} is set to zero. When the amplitude of the supply voltage $|v_g|$ is constant, v_{gd} is constant. The output *d*-*q* axis grid voltages in rotating reference frame are expressed by

$$\begin{cases} v_{gd} = |v_g|, \\ v_{gq} = 0. \end{cases} \tag{5.22}$$

For a system with $v_{qs} = 0$ is used for the grid-side converter, the equations of the active and reactive power in rotating reference frame, which is aligned in the utility grid are:

$$\begin{cases} P_g = \frac{3}{2} v_{gd} i_{gd}, \\ Q_g = -\frac{3}{2} v_{gd} i_{gq}. \end{cases} \tag{5.23}$$

From (5.23), the *q*-axis current is set to variable for reactive power control. The dc power has to be equal to the active power flowing between the utility grid and the dc-link converter. Thus,

$$C_{dc} \frac{d}{dt} V_{dc} = I_{C,dc} = I_{g,dc} - I_{r,dc} \tag{5.24}$$

where V_{dc} is the dc-link voltage, $I_{r,dc}$ is the current between the dc-link and the rotor-side converter, $I_{g,dc}$ is the current between the dc-link and the grid-side converter, and C_{dc} is the dc-link capacitor. Therefore, the *d*-axis current i_{gd} is set by dc-link voltage controller and controls the active power flow between the utility gird and the dc-link.

5.4.2 Grid-connected voltage vector control scheme

Based on the grid-connected voltage vector control, a complete scheme of grid-side three-level NPC VSC controlled of DFIG system is developed and it is indicated in Figure 5.7. This control scheme has three control loops, one external loop to control the dc-link voltage and two internal loops to regulate the *d*-*q* current components, the *d*-axis current component is utilized to regulate the dc-link voltage and the *q*-axis current component is utilized to control the reactive power. The output slip power from DFIG and the power factor of the utility grid can be controlled by changing *d*-axis current and *q*-axis current, respectively.

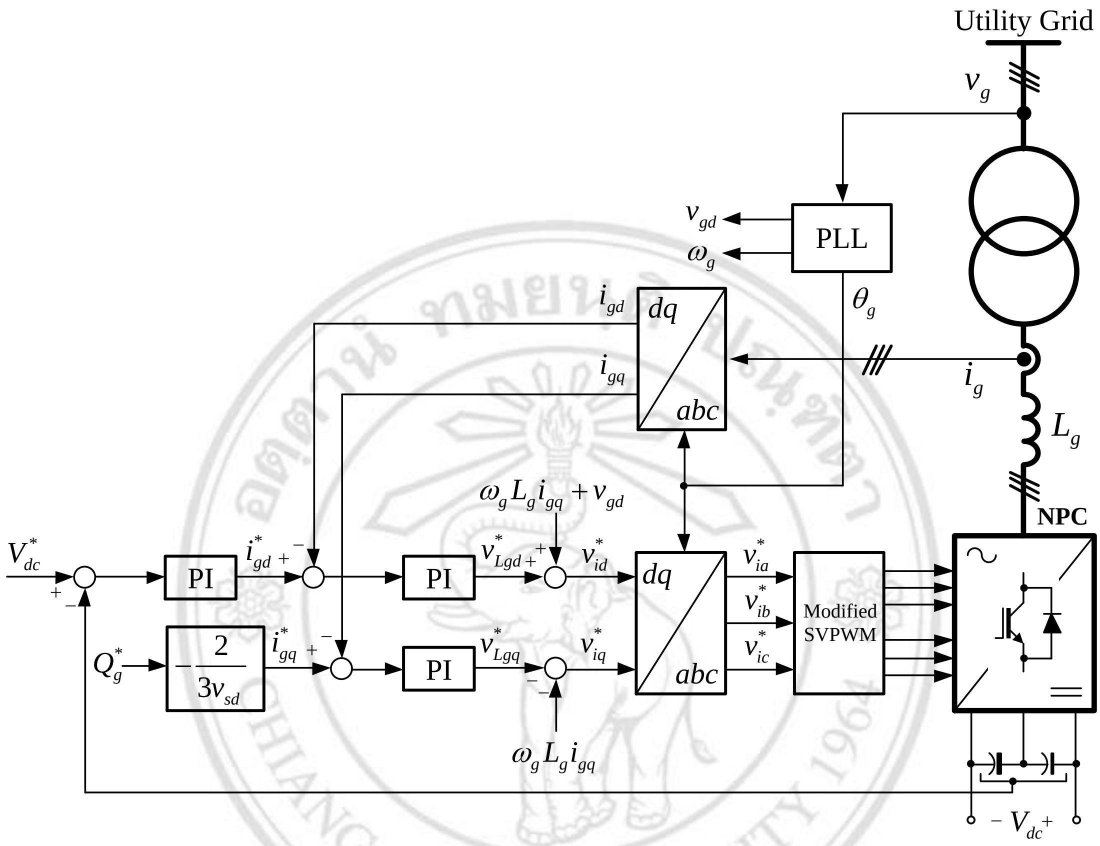

Figure 5.7 Block diagram of grid-side three-level NPC VSC controlled for DFIG system.

As shown in Figure 5.7, the dc link voltage controller is the outer loop, while the current controller is the inner loop. The main objective of the control scheme is to regulate dc-link voltage V_{dc} to follow the reference value V_{dc}^* , while the grid current is sinusoidal shape and either in-phase or out of phase with the utility grid. The dc-link voltage error is delivered to PI dc voltage controller, which generates the reference value of the current in *d*-axis component i_{gd}^* . To achieve the unity power factor condition in the grid-side converter, the referenced current value of *q*-axis component i_{gq}^* is set to zero. The current errors are delivered to PI current controllers that generates the reference voltages v_{id}^*, v_{iq}^*, as,

$$
\begin{cases}
v_{id}^{*} = v_{Lgd}^{*} + \omega_g L_g i_{gq} + v_{gd}, \\
v_{iq}^{*} = v_{Lgq}^{*} - \omega_g L_g i_{gd}.
\end{cases} \tag{5.25}
$$

After transformation into the *abc* reference frame, the reference voltage $v_{ia}^{*}, v_{ib}^{*}, v_{ic}^{*}$ are delivered to the modified SVPWM which generates switching signals for three-level NPC VSC.

5.4.3 Design of dc-link voltage controller

The dc-link voltage controller is used to generate the reference current in *d*-axis component for the current controller. The aim of this controller is to keep the dc voltage constant on the dc-link between the rotor-side and the grid-side converters, which is changed according to balance of power replaced by the converter. The dc voltage loop is the outer loop while the current loop is the inner loop. The design of the dc-link voltage controller has been designed to achieve short settling time and fast correction of the error.

The dc power has to be equal to the active power flowing between the utility grid and the dc-link inverter. Thus,

$$
\begin{cases}
P_{dc} = P_g, \\
V_{dc} I_{g,dc} = \dfrac{3}{2} v_{gd} i_{gd}.
\end{cases} \tag{5.26}
$$

The expression for the average dc-link grid-side current $I_{g,dc}$ is given by

$$
I_{g,dc} = \frac{3}{2} \frac{v_{gd} i_{gd}}{V_{dc}}, \tag{5.27}
$$

The differential equation of the dc-link voltage is expressed as

$$
\frac{d}{dt} V_{dc} = \frac{3}{2} \frac{v_{gd} i_{gd}^{*}}{V_{dc} C_{dc}} - I_{r,dc} \tag{5.28}
$$

Applying Laplace transform to the dc-link voltage control loop in (5.28) one has,

$$C_{dc}sV_{dc}(s)=\frac{3}{2}\frac{v_{gd}i_{gd}^{*}(s)}{V_{dc}}-I_{r,dc}(s) \tag{5.29}$$

The block diagram for the dc-link voltage control is shown in Figure 5.8, in which $I_{r,dc}(s)$ is represented as a disturbance.

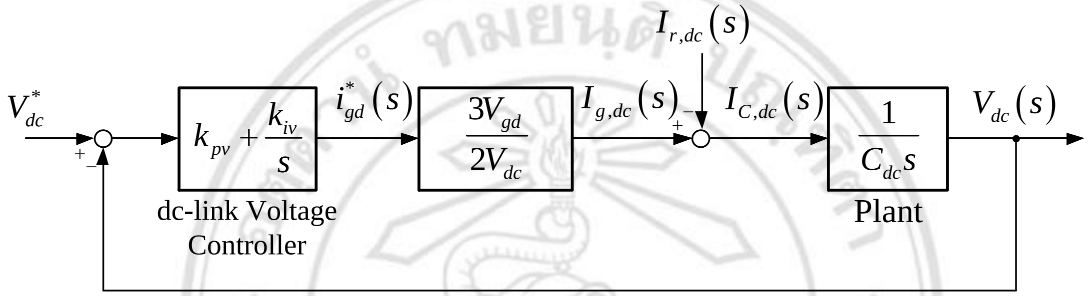

Figure 5.8 Block diagram of the dc-link voltage control loop.

The closed-loop transfer function of the dc-link voltage controller in Figure 5.8 can be written as

$$\frac{V_{dc}(s)}{V_{dc}^{*}(s)}=\frac{\frac{3}{2}\frac{V_{gd}}{V_{dc}C_{dc}}\left(k_{pv}s+k_{iv}\right)}{s^{2}+\frac{3}{2}\frac{V_{gd}}{V_{dc}C_{dc}}k_{pv}s+\frac{3}{2}\frac{V_{gd}}{V_{dc}C_{dc}}k_{iv}}. \tag{5.30}$$

The general form of the characteristic equation of the second-order system for the dc-link voltage controller is given by

$$s^{2}+2\xi\omega_{nv}s+\omega_{nv}^{2}=0, \tag{5.31}$$

where ω_{nv} is the natural angular frequency of dc-link voltage control for $\xi\le 1$ and ξ is the damping ratio.

Therefore, the parameters of PI controller of dc-link voltage control might be calculated as

$$\begin{cases} k_{pv} = \dfrac{2}{3}\dfrac{V_{dc}}{V_{gd}} 2\xi\omega_{nv}C_{dc}, \\ k_{iv} = \dfrac{2}{3}\dfrac{V_{dc}}{V_{gd}} \omega_{nv}^2 C_{dc}. \end{cases} \tag{5.32}$$

5.4.4 Design of grid-connected current controller

The *d*-axis and *q*-axis current controllers have the same dynamic controls. Considering (5.21) with the *d*-axis of rotating reference frame aligned to the utility grid voltage vector, the following relationship can be obtained:

$$\begin{cases} v_{gd} = R_g i_{gd} + L_g \dfrac{d}{dt} i_{gd} - \omega_g L_g i_{gq} + v_{id}, \\ 0 = R_g i_{gq} + L_g \dfrac{d}{dt} i_{gq} + \omega_g L_g i_{gd} + v_{iq}. \end{cases} \tag{5.33}$$

From (5.33), the grid-side inductance voltages are specified as,

$$\begin{cases} v_{Lgd}^* = R_g i_{gd} + L_g \dfrac{d}{dt} i_{gd}, \\ v_{Lgq}^* = R_g i_{gq} + L_g \dfrac{d}{dt} i_{gq}. \end{cases} \tag{5.34}$$

By Laplace transform, the voltage equations can be expressed as

$$\begin{cases} v_{Lgd}^*(s) = R_g i_{gd}(s) + L_g s i_{gd}(s), \\ v_{Lgq}^*(s) = R_g i_{gq}(s) + L_g s i_{gq}(s). \end{cases} \tag{5.35}$$

The transfer function of the current loop can be written as

$$\frac{i_{gd}(s)}{v_{Lgd}^*(s)} = \frac{i_{gq}(s)}{v_{Lgq}^*(s)} = \frac{1}{R_g + L_g S}. \tag{5.36}$$

Equation (5.36) shows that the relationship between grid-side current and the grid inductance voltage is equivalent to a first order system. The PI controller for achieving good performance of tracking the *d*-*q* reference current signals can be synthesized for the desired closed-loop transfer function.

Therefore, the closed-loop transfer function of the current controller in Figure 5.9 can be written as

$$\frac{i_{rd}^{*}(s)}{i_{rd}(s)} = \frac{i_{rq}^{*}(s)}{i_{rq}(s)} = \frac{\dfrac{k_{pi}s + k_{ii}}{L_g}}{s^2 + \dfrac{R_g + k_{pi}}{L_g}s + \dfrac{k_{ii}}{L_g}} \tag{5.37}$$

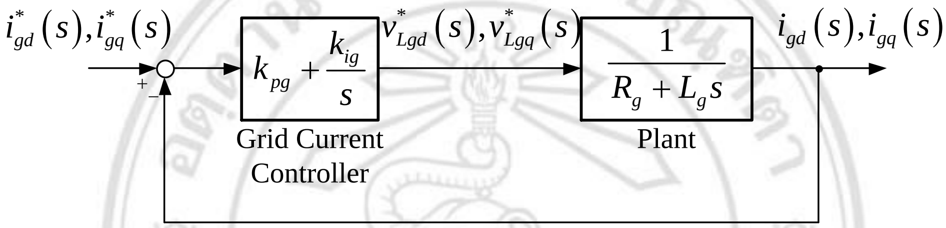

Figure 5.9 Block diagram of the grid-connected current control loop.

The general form of the characteristic equation of the second-order system for the grid-connected current controller is given by

$$s^2 + 2\xi\omega_{ni}s + \omega_{ni}^2 = 0 \tag{5.38}$$

where ω_{ni} is the natural angular frequency of current control for $\xi \le 1$ and ξ is the damping ratio.

Therefore, the parameters of PI controller of grid-connected current control might be calculated as

$$\begin{cases} k_{pi} = 2\xi\omega_{ni}L_g - R_g, \\ k_{ii} = \omega_{ni}^2 L_g. \end{cases} \tag{5.39}$$

5.4.5 Phase-locked loop

When connecting a grid-side converter to the utility grid, it is important to have fast and accurate measurement of the grid phase angle in order to control the active and reactive power flow of the grid-side converter. Consequently, a phase-locked loop (PLL) is implemented in the grid-connected control [54]. The PLL is used in order to determine the phase angle and the frequency of the utility grid.

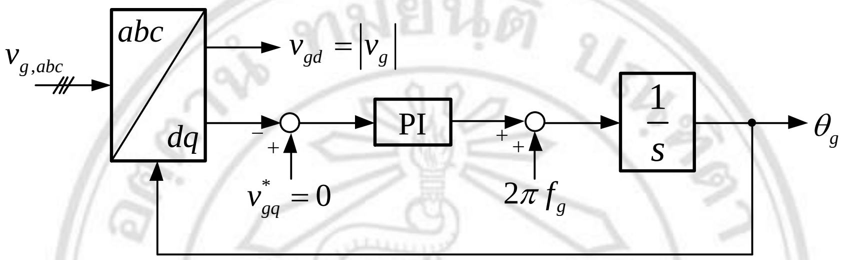

Figure 5.10 Block diagram of a utility grid phase-locked loop.

Figure 5.10 shows the block diagram of the PLL. The inputs of PLL are the three-phase grid voltages and the output is the grid phase angle. The *q*-axis grid voltage component is set to zero, which locks the grid phase voltage. The PI controller is used to minimize *q*-axis grid voltage component to zero, which is integrated in order to obtain the grid phase angle. The transfer function of the PLL is of second order and can be expressed as

$$\frac{\theta_g}{\theta_g^*} = \frac{k_{p,PLL}s + k_{i,PLL}}{s^2 + k_{p,PLL}s + k_{i,PLL}}, \tag{5.40}$$

where θ_g^* is the reference grid phase angle, θ_g is the grid phase angle, $k_{p,PLL}$ is the proportional gain of PLL, and $k_{i,PLL}$ is the integral gain of PLL.

Figure 5.11 shows the experimental waveforms of the three-phase grid voltage and grid phase angle. It can be seen that the phase angle and grid phase voltage in phase *a* varies from 0 to 2π periodically.

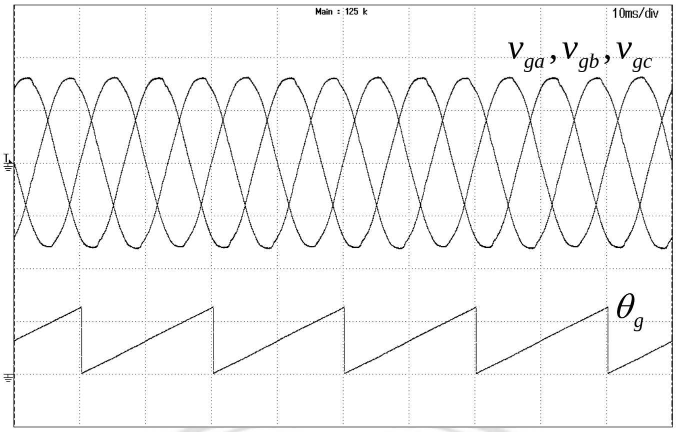

Figure 5.11 Experiment waveforms of utility grid angle for PLL scheme.

5.5 Simulation results

Simulations of the stator voltage vector control scheme for a DFIG system based on three-level NPC VSC have been developed using Matlab/Simulink in order to evaluated performance. The DFIG is rated at 1 kW, with parameters listed in Table 2.1. The nominal dc-link voltage is 180 V, which is controlled by dc-link voltage controller in the grid-side converter, and the switching frequency for both the grid-side and rotor-side converters is 2.5 kHz. In order to show the stator voltage vector control scheme for DFIG system, the simulations have been carried out under the following conditions.

5.5.1 Dynamic response in sub-synchronous speed

In Figure 5.12, the sub-synchronous speed at 1200 rpm and reactive power steps are carried out to simulate the dynamic response of the stator voltage vector control scheme. The stating speed is set to constant, which is generated by the constant torque command T_e^* for constant stator active power P_s, and the stator reactive power reference Q_s^* is set to 0 VAR for unity power factor. The performance of the various proposed control schemes are evaluated by reference unit step responses where the stator reactive power reference is changed from zero to +300 VAR at 1.0 s and from +300 to -300 VAR at 1.1 s, respectively.

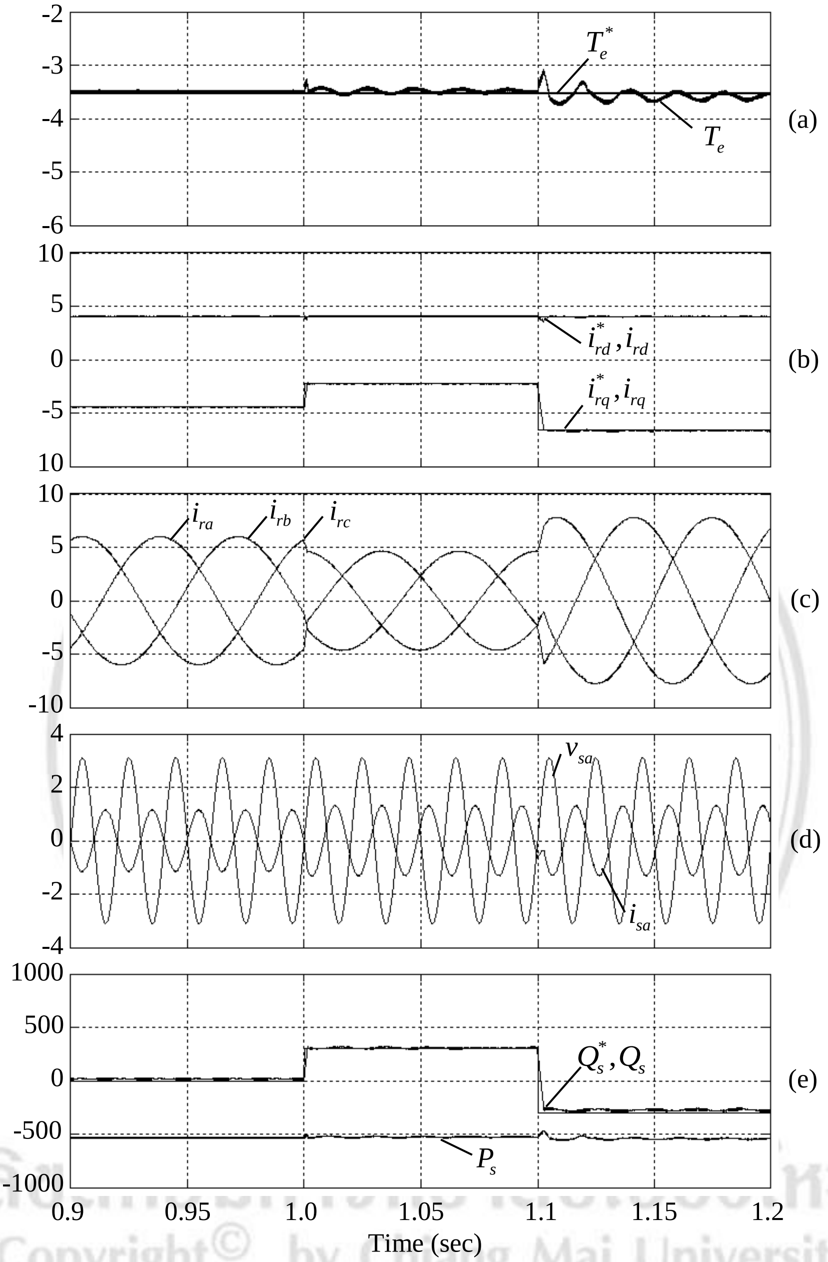

Figure 5.12 Simulation results under constant stator active power and various stator reactive power steps in constant sub-synchronous speed.

Figure 5.12 (a) shows the electromagnetic torque reference T_e^* and the electromagnetic torque of the generator T_e. It can be seen that the electromagnetic torque of generator is regulated to the reference torque, around -3.5 Nm. Figure 5.12 (b) shows the rotor current reference components i_{rd}^*, i_{rq}^* and the measured rotor current components i_{rd}, i_{rq} in *d-q* rotating reference frame. As can be seen from results, the d-axis rotor current i_{rd} follows the rotor current reference i_{rd}^*, while the q-axis rotor current i_{rq} is maintained at its constant reference value i_{rq}^*. The three-phase rotor currents in sub-synchronous speed are shown in Figure 5.12 (c). The simulated waveforms for the stator-side of generator are shown in Figure 5.12 (d). For $Q_s^* = 0$ during $0.9 < t < 1.0$ s, the waveforms of the stator voltage v_{sa} and stator current i_{sa} are out of phase, the generator is operated in the generating mode with unity power factor. The stator active power delivered to the utility grid. From Figure 5.12 (e), the reactive power reference is changed to from zero to +300 VAR at during $1.0 < t < 1.1$ s. It can be seen that the stator current i_{sa} lags the stator voltage v_{sa}. This power factor operation, the generator receives the reactive power from the utility grid. After 1.1 s, the reference of the stator reactive power is changed to -300 VAR. The stator current i_{sa} leads the stator voltage v_{sa}, demanding a leading power factor operation. The generator delivers the reactive power to the utility grid. Finally, the DFIG system response during step change of reactive power is performed and the simulated results are shown in Figure 5.12 (e). The stator reactive power is step changed with from 0 VAR, +300 VAR, and -300 VAR, with the stator active power kept constant.

5.5.2 Dynamic response in super-synchronous speed

In Figure 5.13, the performance with super-synchronous speed at 1800 rpm and reactive power steps were carried out to simulation the dynamic response of the stator voltage vector control scheme. This condition is generated by the constant torque command T_e^* for constant stator active power P_s, and the stator reactive power reference Q_s^* is set to 0 VAR for unity power factor and changed to +300 VAR at 1.0 s and from +300 to -300 VAR at 1.1 s, respectively.

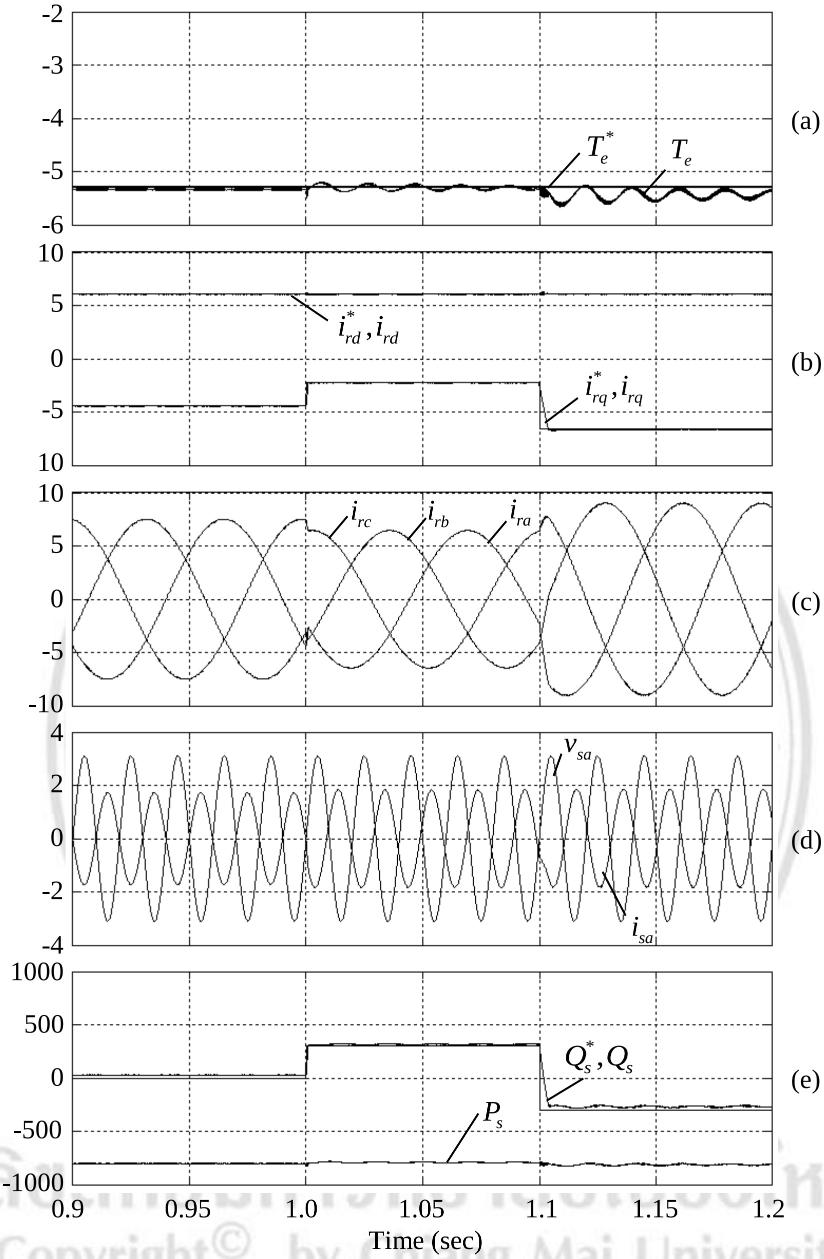

Figure 5.13 Simulation results under constant stator active power and various stator reactive power steps in constant super-synchronous speed.

Figure 5.13 (a) shows the electromagnetic torque reference T_e^* and the electromagnetic torque of the generator T_e. It can be seen that the electromagnetic torque of generator is equal to the reference torque, around -5.3 Nm. Figure 5.13 (b) shows the rotor current reference components i_{rd}^*, i_{rq}^* and the measured rotor current components i_{rd}, i_{rq} in *d*-*q* rotating reference frame. It can be seen that the d-axis rotor current i_{rd} follows the rotor current reference i_{rd}^{*}, while the q-axis rotor current i_{rq} is maintained at its constant reference value i_{rq}^{*}. The three-phase rotor currents in sub-synchronous speed are shown in Figure 4.7 (c). In Figure 4.7 (d), the stator current i_{sa} lags the stator voltage v_{sa}, during $1.0 < t < 1.1$ s. The DFIG receives the stator reactive power from the utility grid. After 1.1 s, the reference of the stator reactive power is changed to -300 VAR. The stator current i_{sa} leads the stator voltage v_{sa}. Finally, the simulated results during step change of reactive power are shown in Figure 4.7 (e). The stator reactive power is step changed with the stator active power kept constant at 795 W.

5.5.3 Dynamic response in speed change

The performance of the DFIG system using back-to-back three-level NPC VSC is observed when the rotor speed varied by 20% slip, as shown in Figure 5.14. Figures 5.14 (a) and (b) show the rotor speed n_r and slip angle θ_{sl} when rotor speed is ramp up from 1200 to 1800 rpm. It can be seen that the rotor angle position is during acceleration through synchronous speed. Figure 5.14 (c) shows the electromagnetic torque reference T_e^{*} and the electromagnetic torque of the generator T_e. It can be noted that the electromagnetic torque of generator produced by rotor speed is regulated to the reference torque. The waveforms of rotor phase voltage v_{ra} and the dc-link voltage v_{dc}, which is generated by the rotor-side converter, are shown in Figure 5.14 (d). It can be seen that the frequency of the rotor voltage is depending on the rotor speed. Figure 5.14 (e) shows the inverter phase voltage of grid-side converter v_{ia} together with dc-link voltage v_{dc}. It can be observed that the frequency of the phase voltage is constant as utility grid frequency.

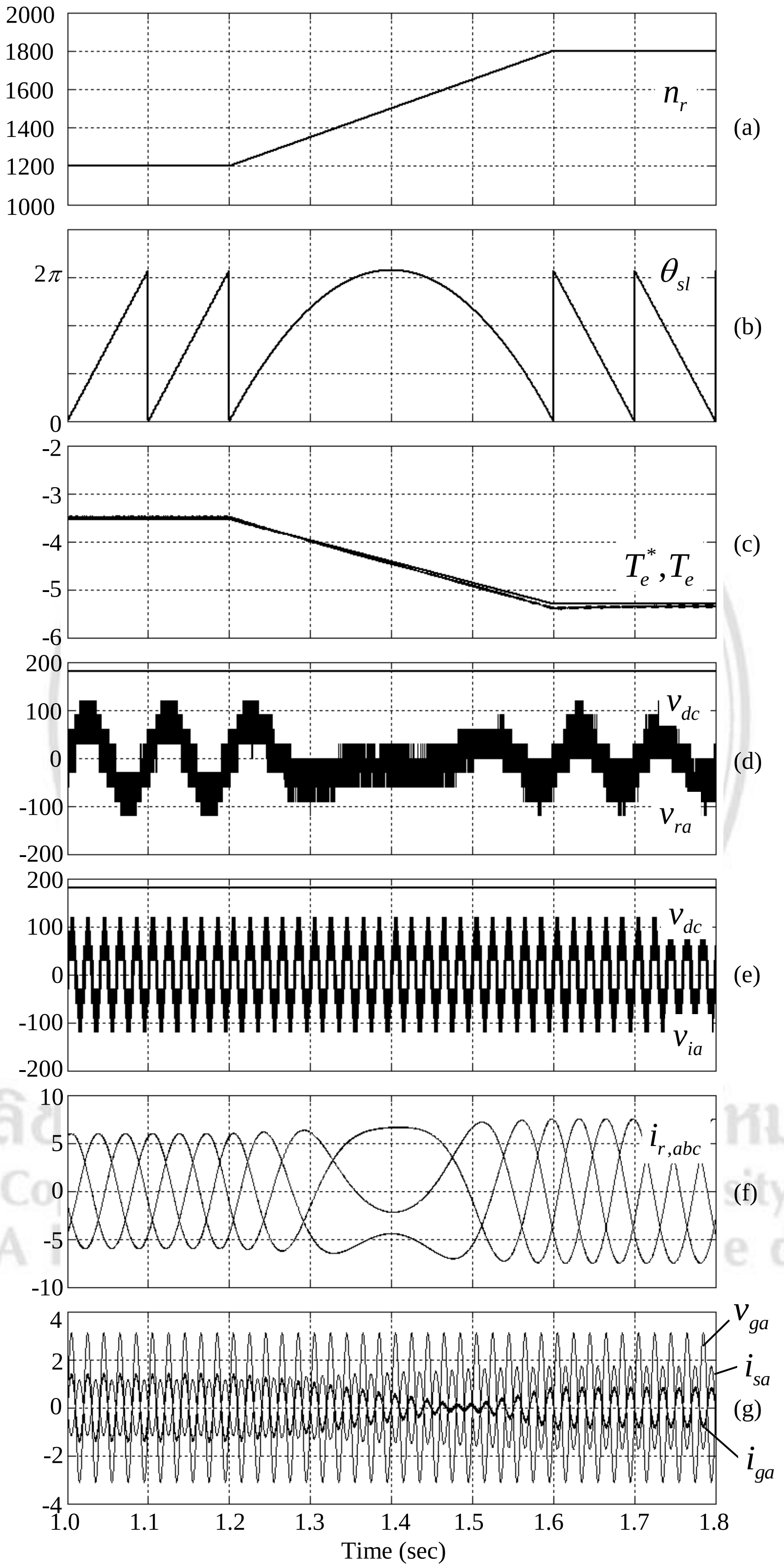

Figure 5.14 Simulation results under varying the stator active power during rotor speed variation.

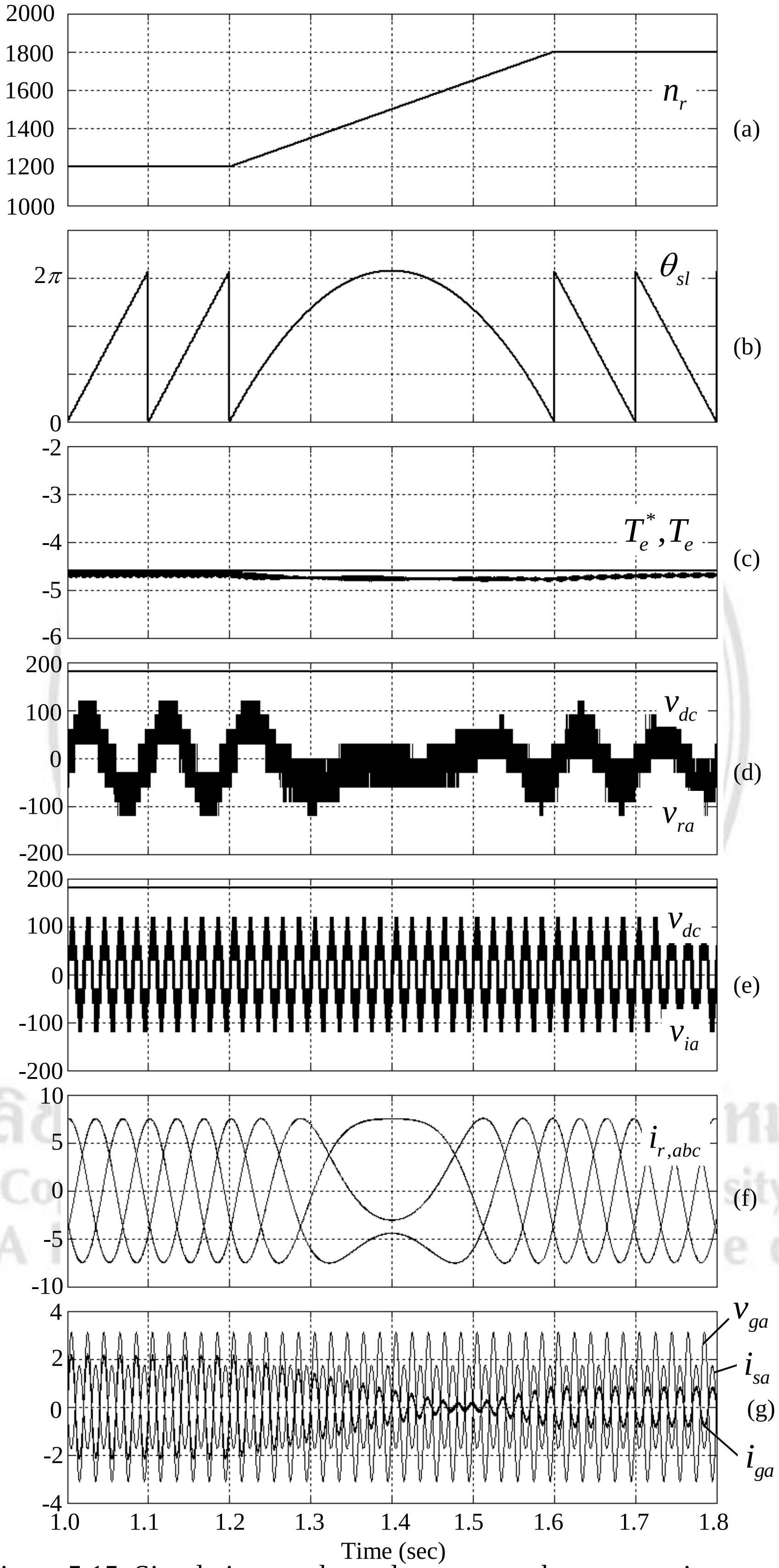

Figure 5.15 Simulation results under constant the stator active power during rotor speed variation.

Figure 5.15 shows the performance of the DFIG system under constant the stator active power during speed variation and reactive power is kept to zero by the controller for unity power operation. Figures 5.15 (a) and (b) show the rotor speed n_r and slip angle θ_{sl} when the rotor speed is ramp up. It can be noted that the slip angle varies periodically when the generator operates during the speed change. Figure 5.15 (c) shows the electromagnetic torque reference T_e^* and the electromagnetic torque of the generator T_e. It can be seen that the generator torque is kept constant at the rated torque under varying the rotor speed change, which follows the reference torque. The waveforms of rotor phase voltage v_{ra} and dc-link voltage v_{dc}, which is generated by the rotor-side three-level NPC VSC, are shown in Figure 5.15 (d) and Figure 5.15 (e) shows the inverter phase voltage of grid-side converter v_{ia} together with dc-link voltage v_{dc}. The line-to-phase voltage of the rotor-side and grid-side converters has seven voltage levels. The three-phase rotor currents i_{ra}, i_{rb}, i_{rc} are shown in Figure 5.15 (f). It is clear that the rotor frequency changes as a function of the magnitude of the rotor slip. Figure 5.15 (g) shows the grid phase voltage v_{ga}, the stator current, i_{sa} and the grid current i_{ga}. In the steady state performance at sub-synchronous speed of the generator at during 1.0 < t < 1.2 s., the phase displacement between the grid phase voltage v_{ga} and the grid current i_{ga} of the grid-side converter is in phase when operated in the rectifying mode. In this operation mode, the grid active power flows into the dc-link. During 1.6 < t < 1.8 s, the waveforms show the grid-side operating in the inverting mode, which corresponds to the super-synchronous speed of the generator. In this operation mode, the grid active power flows from the dc-link into the utility grid. The difference of the grid phase current under speed change is due to the fact that the power consumption in the generator has opposite during sub- and super-synchronous speed operations. For both operation modes, it can be observes that the stator current is out of phase with the utility which the stator active power delivered to the utility grid.

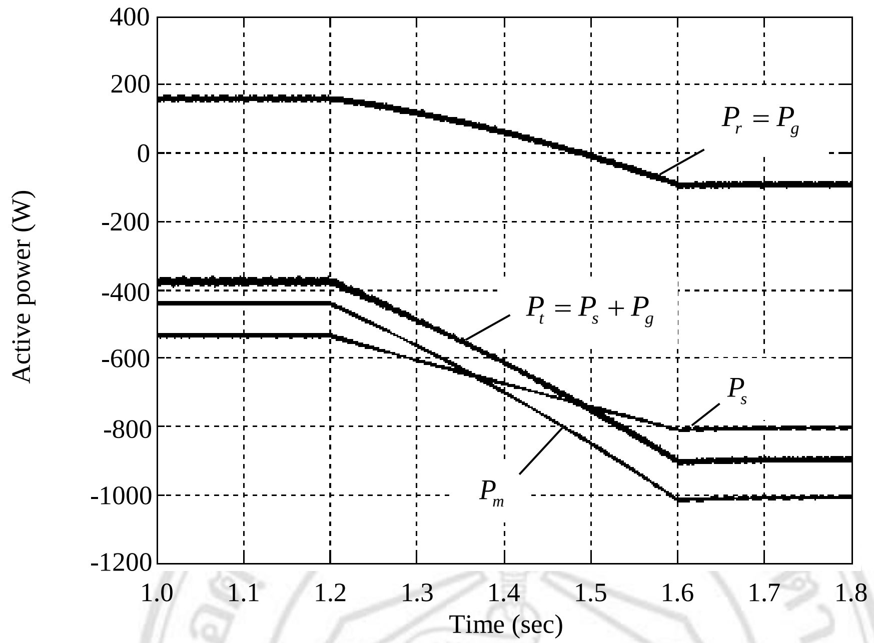

Figure 5.16 Simulation results of active power under speed change with stator active power variation.

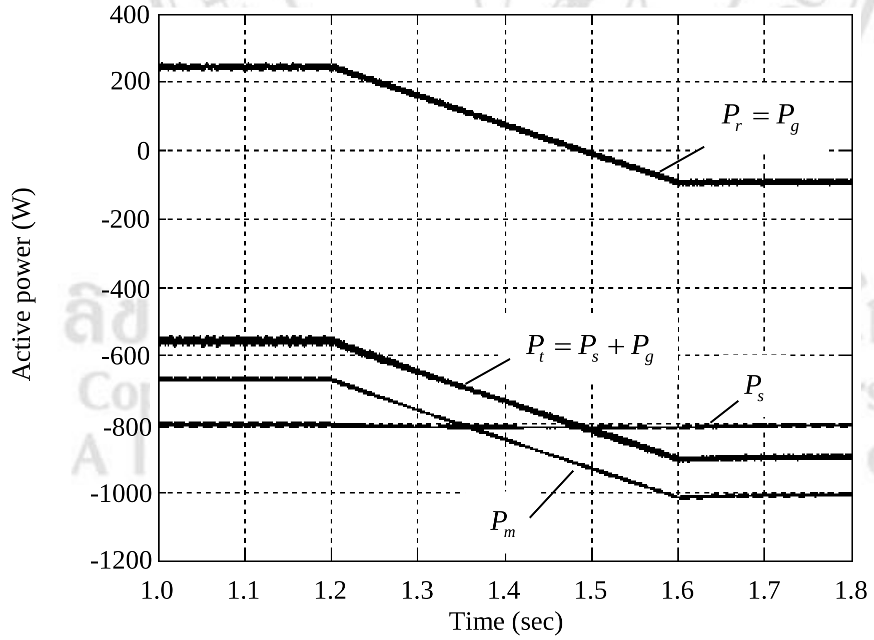

Figure 5.17 Simulation results of active power under speed change with stator active power constant.

Finally, the simulated waveforms of the relationship between the active power of the DFIG system in sub- and super synchronous speed operations are shown in Figure 5.16 and Fig 5.17, respectively. Figure 5.16 shows the relationship between the mechanical power P_m, the stator active power P_s, the grid-side active power P_g and the total active power of the DFIG system P_t under speed change condition from 1200 to 1800 rpm. It can be seen that the variations of the active power are depending on the rotor speed. Figure 5.17 shows the relationship of the active power waveforms of the DFIG system under speed variation. These simulated waveforms show the same as Figure 4.11. It shows that the stator active power is kept constant during speed variation.

5.6 Conclusion

In this chapter, the DFIG system is controlled by the back-to-back three-level NPC VSC. The three-level NPC VSC is controlled by the modified CB-PWM strategy, which has been presented in Chapter 3. The rotor-side and the grid-side converter controllers based on the stator/grid voltage vector control scheme has been presented. In the rotor-side converter controller, the stator active and reactive powers are controlled using the rotating reference frame aligned with the stator voltage. The stator active and reactive powers are controlled with *d*-axis and *q*-axis rotor currents, respectively. The dynamic and steady-state performance behavior of the DFIG system has been investigated by simulations. The performance simulations are able to a good dynamic responses and high accuracy to the active and reactive power control. Finally, the DFIG system using a back-to-back three-level NPC VSC based on the modified CB-PWM strategy was improved the waveform of voltage outputs, reduces the harmonic content compared to the conventional converter, increases the power rating and decreases the stress across the switches.